Parametrisation and use of a predictive DFN model for a high-energy NCA/Gr-SiOx battery

Alana Zülke[1,2,*], Ivan Korotkin[2,3], Jamie M. Foster[2,4],
Mangayarkarasi Nagarathinam[1], Harry Hoster[1,2], and Giles Richardson[2,3]

[1]*Department of Chemistry, Lancaster University, Lancaster, LA1 4YB, UK*
[2]*The Faraday Institution, Quad One, Harwell Campus, Didcot, OX11 0RA, UK*
[3]*Mathematical Sciences, University of Southampton, University Rd., SO17 1BJ, UK*
[4]*School of Mathematics and Physics, University of Portsmouth, Lion Terrace, PO1 3HF, UK*
[*]*Corresponding author:* `a.zulke@lancaster.ac.uk`

November 29, 2021

Abstract

We demonstrate the predictive power of a parametrised Doyle-Fuller-Newman (DFN) model of a commercial cylindrical (21700) lithium-ion cell with NCA/Gr-SiOx chemistry. Model parameters result from the deconstruction of a fresh commercial cell to determine/confirm chemistry and micro-structure, and also from electrochemical experiments with half-cells built from electrode samples. The simulations predict voltage profiles for (i) galvanostatic discharge and (ii) drive-cycles. Predicted voltage responses deviate from measured ones by <1% throughout at least ∼95% of a full galvanostatic discharge, whilst the drive cycle discharge is matched to a ∼1-3% error throughout. All simulations are performed using the online computational tool DandeLiion, which rapidly solves the DFN model using only modest computational resource. The DFN results are used to quantify the irreversible energy losses occurring in the cell and deduce their location. In addition to demonstrating the predictive power of a properly validated DFN model, this work provides a novel simplified parametrisation workflow that can be used to accurately calibrate an electrochemical model of a cell.

Keywords: Li-ion battery modelling, Newman model, P2D model, Drive-cycles simulation.

1 Introduction

Lithium ion batteries (LiBs) are likely to remain the main energy storage technology powering portable electronics, stationary energy storage units and electric vehicles over the next few decades. Furthermore, the share of the automotive market held by electric vehicles is predicted to carry on growing precipitately. The continued rapid growth in the LiB market has provided the drive for a swift expansion in lithium battery sub-technologies that are being brought from the lab onto the market; these include the development of new electrode materials, cell designs and cell chemistries. Despite these new developments in materials and cell architecture, the physics underpinning the operation and ageing of these devices, remains essentially unchanged.

The efficient design of LiBs requires a fundamental understanding of the key physical phenomena, and mathematical models encapsulate the interactions between these phenomena within the complex structure of the device.

In this context, accurate physics-based models of battery performance are extremely valuable and have the potential to yield significant competitive advantage to battery developers with an active R&D program. The seminal works of Doyle, Fuller and Newman in the 90's [1, 3, 2] led to the development of thermodynamically consistent pseudo-two dimensional (P2D) battery models. At the battery pack scale, or even that of a cylindrical or a pouch cell, phenomenological equivalent circuit models (EQC) [4] are often used (instead of physics-based models) because of the high computational cost of simulating multiple copies of the P2D model in a thermally heterogeneous three-dimensional structure. However these phenomenological models, often termed as "black boxes", cannot be directly related to the chemistry occurring within the battery micro-structure and lead to increased errors especially at the extremes of state-of-charge (SoC). [5] They are thus restricted to a narrow range of current draws and, furthermore, do not allow the possibility of exploring how changes to the cell design affect overall battery performance. The P2D model, which we hereafter referred to as the Doyle-Fuller-Newman (DFN) model, is widely employed in commercial toolboxes such as COMSOL Multiphysics or Dassault's Dymola software and solves the governing equations with algorithms that are carefully designed to ensure the overall conservation of lithium within the device [6, 7]. At an even more detailed level simulations of lithium transport can be performed on electrode particle geometries extracted from microscopy measurements conducted on real electrode geometries, see for example [8], though these are extremely computationally expensive and certainly are no better at fitting to discharge data from real cells than is the DFN model.

In contrast to other modelling approaches, the implementation of DFN models guarantees i) higher accuracy over other traditionally faster and easier simulation approaches, such as equivalent circuits, and ii) does not require large data-sets, a fundamental aspect of purely data-driven approaches using machine learning algorithms, for instance. P2D models are limited however, by the user's access to an extensive list of input parameters describing the internal components of the system in terms of design and geometry, transport and kinetics properties [9].

Extracting the parameters and functions required by the DFN model is an expensive and time-consuming task but nonetheless necessary for full physics-based simulations. Studies that conduct such parameter estimation can be divided into two broad groups: those that assume linear diffusivity of lithium ion transport in the electrode materials (see, for example, [10, 11, 12, 13, 14, 15, 16, 17]) and those that assume a nonlinear diffusion law in the electrode materials (see, for example, [18, 19]). Adopting the former approach leads to a relatively simple parametrization problem. However, it cannot be expected that the DFN (thus parametrised) will agree well with experiment across the full spectrum of battery operation, simply because lithium transport in most electrode materials is highly nonlinear. Some authors try to overcome this limitation by introducing an element of non-physical fitting; thus, for example, [11] uses the concept of a current dependent electrode particle radius while [17] uses current dependent weighting factors. Despite some success achieved by adopting these strategies, the optimal parametrization techniques require that lithium diffusivity in the electrode materials is quantified as a function of local lithium concentration. This is usually achieved by performing galvanostatic intermittent titration technique (GITT) or electrochemical impedance spectroscopy (EIS) (see, for example, Ecker *et al.* [19]), potentiostatic intermittent titration technique (see, for example, Oca *et al.* [18]) or by applying the Randle's Sevick equation on cyclic voltammetry data obtain at different sweep rates. The linear diffusivity approximation can work well without *ad-hoc* non-physical fitting procedures but only where comparison is made to a restricted range

of the batteries state of charge, for example for drive cycles which operate in a constrained region (*e.g.* [10, 13, 16]).

Physics-based modelling has often been claimed to be 'too computationally expensive', and therefore impractical, for battery management systems (BMS). However, the recent development of linear scaling algorithms, with compiled language and cloud-based data management to solve the DFN model means that this is no longer true. In this context, we mention the package DandeLiion [20, 21] which overcomes the aforementioned limitations and provides a standalone solution to solve the DFN model in a user-friendly way.

Besides, P2D models can be potentially combined to other modelling techniques creating corrugated models of even faster performance. The research has seen substantial increased interest for the hybridisation of modelling techniques since physics-based models are known to improve accuracy and do not require large data-pools, ultimately yielding decreased degradation rates of the batteries with obvious financial and environmental implications [22]. It has been recently reported that the coupling of P2D solvers to electrochemical observers in state of charge and remaining useful life (SOC/RUL) algorithms for instance, evidencing the enormous potential of physics-based modelling for the battery industry [23].

The purpose of this paper is twofold: firstly, to demonstrate how the DFN model parameters can be determined efficiently by experiments conducted on a real cell; and, secondly, to show that solutions obtained from a DFN model parametrised in this fashion are capable of accurately predicting the cell's dynamic behaviour for different discharge protocols, including both constant current discharges and full drive cycles, which encompass both fully charged and fully discharged states of the battery. Our work thus extends that of Ecker *et al.* [19, 24] which performs a careful parametrisation but does not make the comparison to full drive cycles. In order to accomplish these goals we parametrised a 21700 cell composed of lithium-nickel-cobalt-aluminium oxide (NCA) as cathode and graphite-silicon oxide (Gr-SiOx) as anode material and then used our parameter set in DandeLiion to make predictions of galvanostatic and a drive-cycle discharges. The accuracy of the parametrised model is quantified via the absolute differences between simulated and experimentally measured voltage profiles during discharge. To our knowledge, no other DFN parametrisation of a complete NCA/Gr-SiOx system exists in the literature, despite these batteries being widely employed in the automotive sector, *e.g.* on Tesla's model 3 cars [25]. We also discuss the main approximations made in our model and introduce a simplified experimental workflow for the required parametrisation process. By providing relevant data and a set of comprehensive guidelines on the parametrisation and usage of DandeLiion, we hope to catalyse the widespread use of electrochemical models in both academic research and industry alike.

2 The DFN model

The internal structure of LiB electrodes are intricate and the processes that allow them to store, and release, energy effectively comprises of various length scales. As shown in figure 1, both the anode and cathode are comprised of relatively small ($\sim 10^{-6}$ m) electrode particles bound together by a polymer binder network, into which carbon black particles are embedded to improve its electrical conductivity. The resulting porous material (comprised of electrode particles and binder) is bathed by a liquid electrolyte. Both electrodes have typical thicknesses on the order of $\sim 10^{-4}$ m, and are therefore many times wider than the dimensions of the electrode particles that are incorporated into their structure, which have typical diameters of a few microns or less. Obtaining solutions to partial differential equations posed on a geometry with such disparate
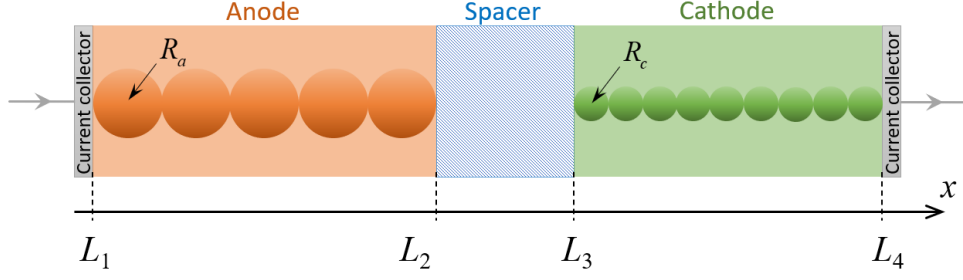
Figure 1: Schematic of a planar Li-ion battery cell

length scales is computationally expensive and, even where this is possible, is hindered by the difficulty in obtaining a precise specification of the geometry of the electrode structure from microscopy data. DFN is a multiscale modelling framework that circumvents some of these difficulties by posing the model on representative (usually spherical) electrode particles and using an averaged (or homogenised) representation of the electrolyte. The microscale of this multiscale model is associated with lithium transport taking place within individual electrode particles while the macroscale is associated with transport processes taking place on the cell scale, in particular in the electrolyte. The complexity of the pore geometry is retained in the multi-scale equations in the form of 'effective' coefficients which are determined by the microstructure. In the original papers by Newman and coworkers [1, 3, 2] the multi-scale system was posited on an ad-hoc basis, but the model equations have since been systematically derived from much more rigorous arguments in asymptotic homogenisation [26, 27]. In the remainder of this section we shall outline the model and briefly discuss the physical principles that underpin each of the equations.

Macroscopic equations   There are two important charge transport processes that must be captured on the macroscopic scale, namely: (i) ionic conduction in the electrolyte, and (ii) electron conduction in the solid network of electrode particles, binder and additives. The former process is captured in the following equations:

$$\epsilon_l(x)\frac{\partial c}{\partial t} + \frac{\partial N_-}{\partial x} = 0, \quad N_- = -\mathcal{B}(x)D_\mathrm{e}(c)\frac{\partial c}{\partial x} - (1-t_0^+)\frac{j}{F} \quad \text{in} \quad L_1 < x < L_4. \tag{1}$$

$$\frac{\partial j}{\partial x} = b(x)j_n, \qquad j = -\mathcal{B}(x)\kappa(c)\left(\frac{\partial \Phi}{\partial x} - \frac{2RT}{F}\frac{1-t_0^+}{c}\frac{\partial c}{\partial x}\right) \quad \text{in} \quad L_1 < x < L_4, \tag{2}$$

in which c is the concentration of both the positive lithium and negative anions, j is the (averaged) ionic current density, j_n is the transfer current density (from electrode material to electrolyte per unit surface area of electrode material), Φ is the electrolyte potential measured with respect to a lithium reference electrode and N_- is the flux of the negatively charged anions. Our choice to work with N_- is motivated by the fact that anions do not undergo reactions and therefore the anion conservation equation requires no source/sink terms as would be the case for the Li-ion conservation equation;the resulting PDEs are thus more readily discretised, using a finite element method, so as to ensure no artificial loss of lithium occurs in the cell. We note that the DFN model is often stated in an equivalent form in terms of N_+, the flux of Li$^+$ ions. The parameters ϵ_l, $\mathcal{B}$, b, t_0^+ and F are the electrolyte volume fraction, the inverse Mac-Mullin number, the Brunauer–Emmett–Teller (BET) surface area of the electrode particles (*i.e.* the reactive surface area of electrode particles per unit volume of electrode), the transference number and Faraday's constant, respectively. In addition, the functions $D_\mathrm{e}(c)$ and $\kappa(c)$ are the

4

electrolyte diffusivity and the electrolyte conductivity, respectively. Notably ϵ_l, $\mathcal{B}$ and b are effective coefficients that are determined by the properties of the microstructure. Thus, for instance, more tortuous microscale geometries lead to smaller values of $\mathcal{B}$ which captures the retardation of the transport process caused by the tortuosity of the electrolyte paths. Physically, (1a) is a conservation equation for anions whilst (1b) is a constitutive equation for the anions flux N_-. Moreover, (2a) is a charge conservation equation within the electrolyte while (2b) is the constitutive equation for the electrolyte current density, which, in the electrolyte, plays an role analogous to Ohm's Law.

Electron conduction in the solid parts of the electrode matrices are modelled by charge conservation equations and Ohm's Law

$$\frac{\partial j_a}{\partial x} = -b(x)j_n, \quad j_a = -\sigma_a \frac{\partial \Phi_a}{\partial x} \quad \text{in} \quad L_1 < x < L_2, \tag{3}$$

$$\frac{\partial j_c}{\partial x} = -b(x)j_n, \quad j_c = -\sigma_c \frac{\partial \Phi_c}{\partial x} \quad \text{in} \quad L_3 < x < L_4, \tag{4}$$

Here, j_a is the current density in the solid anode matrix, Φ_a is the electric potential in the anode matrix, and σ_a is the effective conductivity in the anode. The analogous variables in the cathode are distinguished by the subscript c.

The transfer current density j_n induced by the redox reactions on the interfaces between the electrode particles and electrolyte are, as usual, given by Butler-Volmer kinetics

$$j_n = \begin{cases} 2Fk_a c^{1/2} \left(c_a|_{r=R_a}\right)^{1/2} \left(c_a^{\max} - c_a|_{r=R_a}\right)^{1/2} \sinh\left(\frac{F\eta_a}{2RT}\right) & \text{in} \quad L_1 \leq x < L_2, \\ 0 & \text{in} \quad L_2 < x < L_3, \\ 2Fk_c c^{1/2} \left(c_c|_{r=R_c}\right)^{1/2} \left(c_c^{\max} - c_c|_{r=R_c}\right)^{1/2} \sinh\left(\frac{F\eta_c}{2RT}\right) & \text{in} \quad L_3 \leq x < L_4, \end{cases} \tag{5}$$

$$\eta_a = \Phi_a - \Phi - U_{eq,a}(c_a|_{r=R_a}), \qquad \eta_c = \Phi_c - \Phi - U_{eq,c}(c_c|_{r=R_c}), \tag{6}$$

where R is the universal gas constant, T is absolute temperature, k_a is the reaction rate constant in the anode, c_a is the concentration of Li within the anode material, $c_a^{\max}$ is the maximum concentration of lithium within the anode material and we assume that the anode particles are spherical with radius R_a. The overpotential and equilibrium overpotential of the anode particles are denoted by η_a and $U_{eq,a}$ respectively. Notably, the condition in which $\eta_a = 0$ is equivalent to equality between the electrochemical potential of a lithium ion in the anode material and that in the electrolyte and so, in turn, is equivalent to the Nernst equation as would be expected when the redox reaction has reached an equilibrium. This may, at first, appear counter-intuitive until one recalls that Φ is not the (Maxwell) electric potential, in the electrolyte, but rather one measured with respect to a lithium reference electrode, from which it follows that $F\Phi$ is the electrochemical potential of a lithium ion in the electrolyte. Counterparts to the anode variables in the cathode are denoted similarly, but with a subscript c.

Macroscopic boundary and interface conditions At the extremities of the cell where the electrodes meet the current collectors there is no flux of anions, no ionic current, and the current in the solid network is equal to that provided/extracted by the external circuit. At the internal interfaces where the anode and cathode meet the separator the current density in the solid network must be zero because the separator is electronically insulating. As such the macroscopic

equations are supplemented by the following boundary conditions

$$j_a|_{x=L_1} = \frac{I(t)}{A}, \quad N_-|_{x=L_1} = 0, \quad j|_{x=L_1} = 0, \tag{7}$$

$$j_a|_{x=L_2} = 0, \tag{8}$$

$$j_c|_{x=L_3} = 0, \tag{9}$$

$$j_c|_{x=L_4} = \frac{I(t)}{A}, \quad N_-|_{x=L_4} = 0, \quad j|_{x=L_4} = 0. \tag{10}$$

where I is the current leaving/entering the cell and A is the area of the contact between the anode/cathode and the current collector.

Microscopic equations and boundary conditions   The interfacial current density j_n depends strongly on the concentration of Li on the surface of the electrode particles necessitating that at every location in the macroscopic dimension, x, we solve an appropriate transport model for the Li within the particles. The transport within the particles occurs on much smaller microscopic scale and we denote radial position within the particle by r. There is considerable debate about the most appropriate equations for describing solid-state transport. In the original papers by Newman and coworkers [1, 3, 2] a linear (Fickian) diffusion model was assumed, but since most sophisticated models, including Cahn-Hilliard [29, 30, 31, 32], and nonlinear diffusion models [33] have all been proposed. Here we opt to take the latter approach and use a nonlinear diffusion equation noting that multiple studies have demonstrated the effectiveness of this model in fitting experimental trends [34]. Here we opt for the very simplest microscopic model by assuming that all particles in the anode (or cathode) are identical spheres of equal radius R_a (or R_c). We argue that the SiOx particles in the anode occur in sufficiently small numbers (4.6%) that they do not significantly undermine this assumption. The microscopic equations and boundary conditions are

$$\left.\begin{aligned} \frac{\partial c_a}{\partial t} &= \frac{1}{r^2}\frac{\partial}{\partial r}\left(r^2 D_a(c_a)\frac{\partial c_a}{\partial r}\right) \quad \text{in} \quad 0 < r < R_a \\ \frac{\partial c_a}{\partial r}\bigg|_{r=0} &= 0, \qquad -D_a(c_a)\frac{\partial c_a}{\partial r}\bigg|_{r=R_a} = \frac{j_n}{F} \end{aligned}\right\} \quad \text{in } L_1 < x < L_2, \tag{11}$$

$$\left.\begin{aligned} \frac{\partial c_c}{\partial t} &= \frac{1}{r^2}\frac{\partial}{\partial r}\left(r^2 D_c(c_c)\frac{\partial c_c}{\partial r}\right) \quad \text{in} \quad 0 < r < R_c \\ \frac{\partial c_c}{\partial r}\bigg|_{r=0} &= 0, \qquad -D_c(c_c)\frac{\partial c_c}{\partial r}\bigg|_{r=R_c} = \frac{j_n}{F} \end{aligned}\right\} \quad \text{in } L_3 < x < L_4, \tag{12}$$

where $D_a(c_a)$ and $D_c(c_c)$ are the lithium diffusivities in the anode and cathode particles respectively. Equations (11) and (12) are the nonlinear diffusion equations for the lithium ion concentration in the electrode particles with boundedness conditions on the concentrations which ensure symmetry and zero lithium ion flux at the particle core, and the Neumann boundary conditions on the surfaces of the particles that ensure the fluxes of lithium leaving the electrolyte balances those entering the electrode particles.

Initial conditions   The initial conditions are required for the ionic concentration in the electrolyte as well as the Li concentration in the anode and cathode particles. We set

$$c|_{t=0} = c_0, \quad c_a|_{t=0} = c_{a,0}, \quad c_c|_{t=0} = c_{c,0}. \tag{13}$$

The full cell potential The results of solution to the full cell DFN model can be used to compute the potentials at the anode and cathode current collectors V_a and V_c, respectively via the relations

$$V_a(t) = \Phi_a\big|_{x=L_1}, \qquad V_c(t) = \Phi_c\big|_{x=L_4}. \tag{14}$$

and hence $V(t)$, the potential drop across the full cell,

$$V(t) = V_c(t) - V_a(t). \tag{15}$$

It is this cell voltage that we shall use to make comparisons between the model and experimental data. In the equation above we neglect the ohmic drop between the current collectors since it is relatively small in comparison with the potential difference given by equation 15.

Table 1: The DFN model parameters: (*) measured, (**) fitted, (†) derived analytically, (‡) provided by the manufacturer. The subscript s should be read as $s = a$ in the anode and $s = c$ in the cathode.

Parameter	Units	Anode	Cathode	Separator
Anode/Cathode/Separator thickness (*)	m	7.5×10^{-5}	5.0×10^{-5}	1.65×10^{-5}
Effective particle radius R_s (*)	m	11.2×10^{-6}	5.0×10^{-7}	-
Cell cross-sectional area A (‡)	m^2	0.14112		
Electrolyte volume fraction ϵ_l (*)	-	0.2082	0.2753	0.4914
Inverse MacMullin number $\mathcal{B}$ (†)	-	0.0950	0.1444	0.3445
Transference number t_0^+ [24]	-	0.26		
Particle surface area per unit volume electrode b (†)	m^{-1}	212089	4348000	-
Diffusivity of electrolyte $D_e(c)$ [19]	$m^2 s^{-1}$	Function (Fig. 3)		
Conductivity of electrolyte $\kappa(c)$ [19]	$S\,m^{-1}$	Function (Fig. 3)		
Conductivity in solid σ_s [24]	$S\,m^{-1}$	14	91	-
Maximum Li concentration in solid c_s^{max} (**)	$mol\,m^{-3}$	29400	43100	-
Reaction rate constant k_s (**)	$m^{5/2}mol^{-1/2}s^{-1}$	1.40×10^{-11}	5.0×10^{-10}	-
Equilibrium potential $U_{eq,s}(c_s)$ (*)	V	Fig. 4 (top)		-
Lithium diffusivity in electrode particles $D_s(c_s)$ (*)	$m^2 s^{-1}$	Fig. 4 (bottom)		-
Absolute temperature T (*)	K	298.15		
Initial concentration of Li in electrolyte c_0 [24]	$mol\,m^{-3}$	1000		
Initial concentration of Li in particles $c_{s,0}$ (**)	$mol\,m^{-3}$	24800	400	-

Model parameters. The DFN model described above requires an extensive list of input parameters and functions. Other than universal gas constant R and Faraday's constant F these are listed in Table 1. A primary focus of this work is to obtain these parameters and functions for the cylindrical lithium-ion cell (21700), which has a mixed graphite-SiOx anode and an NCA cathode. Indeed, the parameter values and input functions determined by the experimental component of this study are also given in Table 1. While some of the parameters are

relatively straightforward to obtain, such as Anode/Cathode/Separator thicknesses, others such as the inverse MacMullin number $\mathcal{B}$ are more difficult to ascertain. Accurate parametrisation of the input functions, which represent variables that vary importantly with lithium concentration, such as lithium diffusivities in the anode and cathode particles $D_a(c_a)$ and $D_c(c_c)$, presents an even greater challenge.

Solution of the DFN model using DandeLiion   We use the highly accurate (second-order) solver DandeLiion [21], which is available online at [20], to solve the DFN model. This software readily allows the user to simulate the discharges that we investigate here, namely constant current, GITT and drive-cycle discharges. Furthermore, it is straightforward to re-parametrise and to output simulation data in a suitable form to use for comparison plots against experiment.

3   Experimental characterisation

Cylindrical cells (21700) with 4.8 Ah rated capacity at 25°C upon C/3 discharge rate were used in the present investigation. The main technical specifications as given by the supplier are shown in Table 2 and the experimental workflow used for parametrisation is illustrated by the diagram in Fig 2.
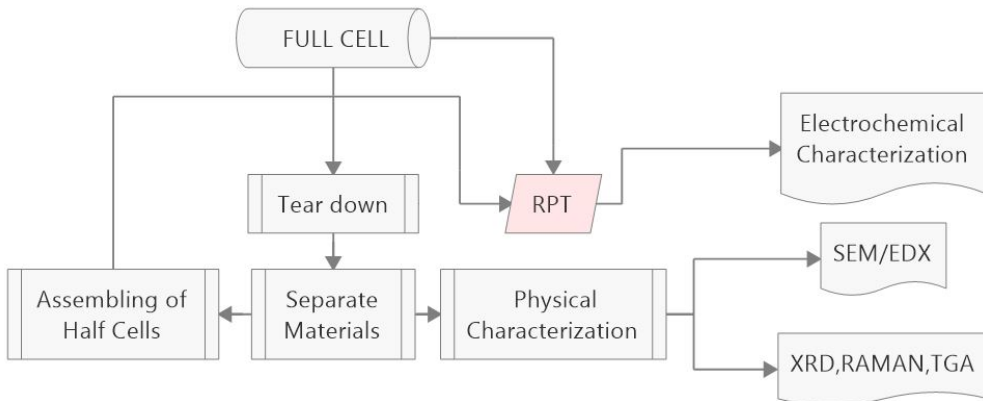

Figure 2: Simplified experimental workflow used for parametrisation of the DFN model.

A thorough parametrisation is time consuming and expensive. Hence it is sensible to first identify the critical model parameters in the particular operating scenario that is to be simulated. By performing a one-at-a-time parameter sensitivity analysis Li *et al.* [35] concluded that simulated drive cycle curves generated by DFN are very sensitive to parameters related to the overall capacity of the battery, such as cathode electrode thickness and active material volume fraction, but are nearly insensitive to electrolyte and separator-related parameters. In contrast, for the simulation of constant current curves, the authors reported different sensitivity depending on the voltage window and C-rates simulated. For instance, the thickness of the cathode has high impact on the simulation of curves at low C-rates, but separator lengths and particle radius are more important at higher C-rates. Motivated by these observations, the experimental workflow proposed here is designed to obtain parameters to a sufficient degree of precision to enable accurate simulations to carried out over a wide range of conditions, such as low-to-moderate constant current discharges and drive-cycles.

---

[1]Mass range as percentage of the total cell mass (g/g) stated in the safety datasheet provided by the supplier.

Table 2: Technical specification

Properties	Specification
Cell type	Cylindrical 21700
Cathode chemistry	Nickel cobalt aluminum oxide (NCA) [20-50% g/g[1]]
Anode chemistry	Graphite/Silicon [10–30% g/g[1]]
Electrolyte salt	Lithium Hexafluorophosphate [0.05–5% g/g[1]]
Electrolyte solvent	Ethylene carbonate, Ethyl methyl carbonate, Dimethyl carbonate [5-20% g/g[1]]
Typical capacity (4.2 V, C/3 discharge)	4.8 Ah
Typical energy (4.2 V, C/3 discharge)	17.4 Wh
Nominal voltage	3.62 V
Lower voltage limit, V_{min}	2.5 V
Upper voltage limit, V_{max}	4.2 V
Energy density	256 Wh/kg; 717 Wh/L
Standard charging current rate	C/3
Maximum charging current rate	1C
Standard discharging current rate	C/5
Maximum discharging current rate	2C
Peak discharging current rate (30 s, 10 s) at 50% SOC and BOL	42 A / 54 A
Cell weight	68 g
Cell dimension	Max. height to top: 70.15 mm Max. height to crimping: 70.15 mm Max. upper diameter: 21.1 mm

Geometric parameters and physical characterisation   The first stage of the parametrisation consists in the tear down of a representative battery sample to reverse-engineer its materials properties. One full cell was completely discharged to 2.5 V, using constant current at C/25, followed by disassembly in a dedicated argon-filled glove box with oxygen content and humidity below 1 ppm (MBraun, MB-Unilab Plus SP). Tear down process begins with the careful removal of the top and insulation caps. Subsequently, the can is cut with a pipe cutter near the groove. The top tabs are disconnected first and carefully peeled off using ceramic pliers. After peeling only, the bottom tabs are disconnected. The electrode foils are then separated from the separator film by unfolding the jelly-roll, having their lengths and masses measured. In our sample, both cathode and anode present double-side coating of total geometric surface area of 1411.2 cm^2 and 1562.4 cm^2 , respectively. Anode electrode foils are typically oversized with regards to the cathode in order to achieve the energy requirement and to limit risks of lithium plating. In this way, anode-to-cathode ratios in commercial cells are always larger than 1. The anode region which has no cathode counter-part is often called overhang area, and lithium movement from/to these regions are known to cause reversible capacity effects taking place at varied time-scales [36].

The chemistry of the active material in the cathode was confirmed to be lithium nickel-cobalt-aluminium oxide by using powder X-ray diffraction (PXRD, Rigaku Smartlab, 9 Kw

Cu source generator, $\lambda \sim 1.54051$ Å). The resulting diffraction spectrum is displayed against a reference spectrum for NCA-80 ($LiNi_{0.8}Co_{0.15}Al_{0.05}O_2$) in the Supplementary Information Fig.S1.

Results from elemental mapping using energy-dispersive X-ray spectroscopy(EDX)/scanning electron microscopy (SEM, JEOL JSM-7800F) confirm that the anode is a mixture of graphite and (SiO_x). Association of other elements allow us to also infer about the presence of ($LiPF_6$) and carboximethylcellulose, commonly used as electrolyte salt and binder material, respectively. In order to estimate the (SiO_x) content, 15 mg of the anode material was mechanically scraped off from the copper current collector foil, using a ceramic scalpel, and placed in a cleaned and tared Al_2O_3 crucible for thermal gravimetrical analysis (NETZSCH STA 449 F3 Jupiter) in N_2/O_2 from 0 to 1100 at 5°C/min. The content of silicon was estimated as 4.6% w/w from the residual mass at $T > 800$°C inferred by TGA (Figure S2) In terms of moles proportionality, this analysis suggest that there is around 45 moles of graphite (carbon graphite, MM = 12 g/mol) to every mol of Si in the anode. Electrodes and separator thicknesses, in addition to particle sizes, were measured from cross-sectional and top-view scanning electron microscopy (SEM). Representative micrographs are displayed in Figure S3. Raw SEM images were turned into binary files and then processed using a conventional image processing software (ImageJ) in order to obtain the distribution of particle sizes by choosing the proper sphericity level for the material being analysed. As the anode is a mixture of graphite and silicon oxide, the average diameter of the Gr-SiOx composites was chosen as the effective (average) anode particle size assuming the Gr/SiOx particles ratio to be 95/5. As part of the set of sensitive information about the product composition, we do not have access to the exact proportion of binder conductive carbon and active material present on the electrodes, so we assume a commonly reported recipe, as 95% of active material for both electrodes. The volume fraction of the electrolyte in the materials was estimated from a combination of top-view and cross-sectional SEM micrographs. This is accomplished by first identifying and confirming the active particle content using the elemental mapping information obtained from the EDX/SEM (Figure S4). EDX/SEM can only be used qualitatively to confirm which elements are present. Subsequently, a threshold range analysis is applied to the binary images to distinguish active particles from the background, to reveal the porosity. Active content of NCA in the cathode inferred by three different images show results varying from 56 up to 73 per cent. Image-based analysis for active content is not a quantitative method and should therefore be used only as an estimate. Using the average background from three different micro-graphs we estimate the volume fraction of electrolyte ϵ_l to be 0.2082, 0.2753 and 0.4914 for anode, cathode and separator, respectively. We stress that these values should be cross-checked whenever possible, with values from porosimetry analysis.

Electrolyte   The inverse MacMullin number $\mathcal{B}$ of the the electrode matrix, which is the reciprocal of the MacMullin number (see *e.g.* [38]) and appears in the electrolyte equations, is estimated from the Bruggeman relation [37]. It is thus related to the volume fraction of electrolyte via

$$\mathcal{B}(x) = (\epsilon_l(x))^{1.5}.$$

Particle surface area per unit volume can then be derived analytically assuming spherical particles with radius $R(x)$,

$$b(x) = 3(1 - \epsilon_l(x))(R(x))^{-1}.$$

We note that the use of the Bruggeman relation to estimate the MacMullin number $\mathcal{B}^{-1}$ has been criticised, *e.g.* in [38], and in particular it tends to overestimate the real value of $\mathcal{B}$.

It is experimentally inaccessible to harvest the electrolyte from the full cell during the tear down process. Conductivity and diffusivity in the electrolyte (Figure 3) were obtained from the data available in Ecker *et al.* [19, 24] by making the assumption that both systems use electrolyte of very similar composition (in both cases $LiPF_6$ dissolved in a carbonate-based solvent).The complete electrolyte composition including the ratio of different solvents and additives are proprietary information, and therefore not available.
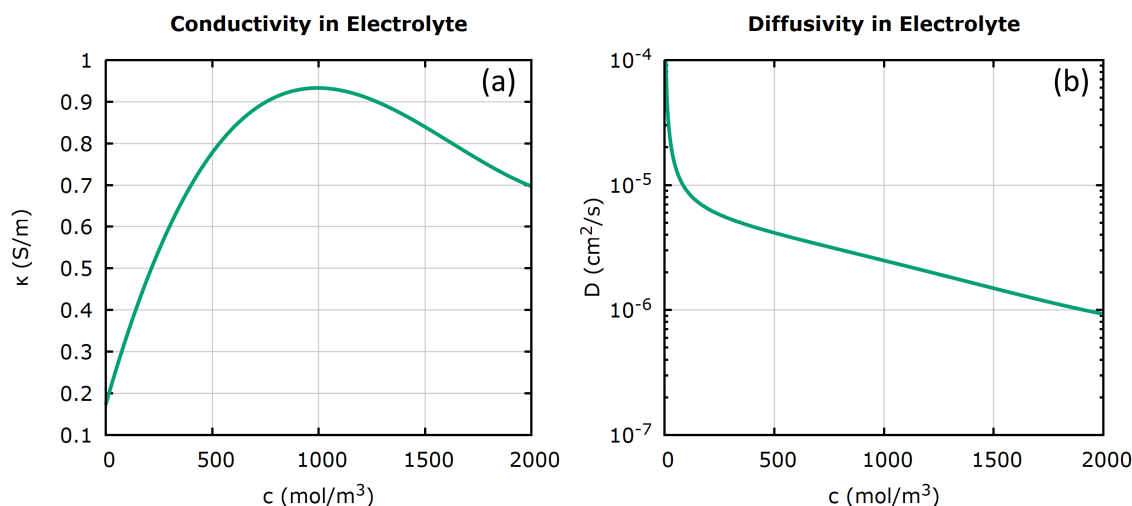
Figure 3: Conductivity (left) and ionic diffusivity (right) of the electrolyte using data provided from [19, 24]

Electrochemical characterisation   In order to extract data on the electrode thermodynamics, kinetics and transport properties we fabricated half-cells in coin cell configurations. This was accomplished by mechanically punching out anode and cathode circles of diameter $d = 19$ mm from the electrode foils (double-side coating) and re-assembling them into CR2032 cells with a metallic lithium counter-electrode. All electrode and separator discs were cut using a small manual die cutting punching machine and assembled by hydraulic crimping (TOB Energy). Fiberglass was used for the separator and a battery grade 1 M $LiPF_6$, in ethylene carbonate/dimethyl carbonate (LP30, Sigma Aldrich), was employed as the electrolyte. No solvent-based cleaning of the electrode foils was conducted in order to avoid removal of the solid electrolyte interphase (SEI) and guarantee minimum interference with the resulting electrochemical response. After a 12-hour rest period for proper wetting of the internal components, three consecutive cycles at C/12 (determined with regards to the active material mass) and 25°C were undertaken for conditioning between 0.05 V and 1.0 V for the anode half-cell and from 3.0 to 4.3 V for the cathode half-cell. Pseudo-OCV curves were then obtained at sufficiently slow constant current and at 25°C. We confirm that a current rate of C/25 yields near-equilibrium voltage profiles by comparing it with the curves at even slower rates, such as C/60 where identical electrochemical signatures are obtained. (Figure S5) The half-cells made from intact harvested material can be used for DFN parametrisation but show poor cyclability, hence can only be used for a few cycles. Only the first five, consecutive and reproducible cycles after conditioning of the coin cells were used in this work. We show the comparison of pseudo-OCV curves obtained at the same very low C-rate and temperature for cathode, anode and full cell as Supplementary Material (Figure S6). Analytical fits for the half-cell anode and cathode (dis)charge voltage profiles
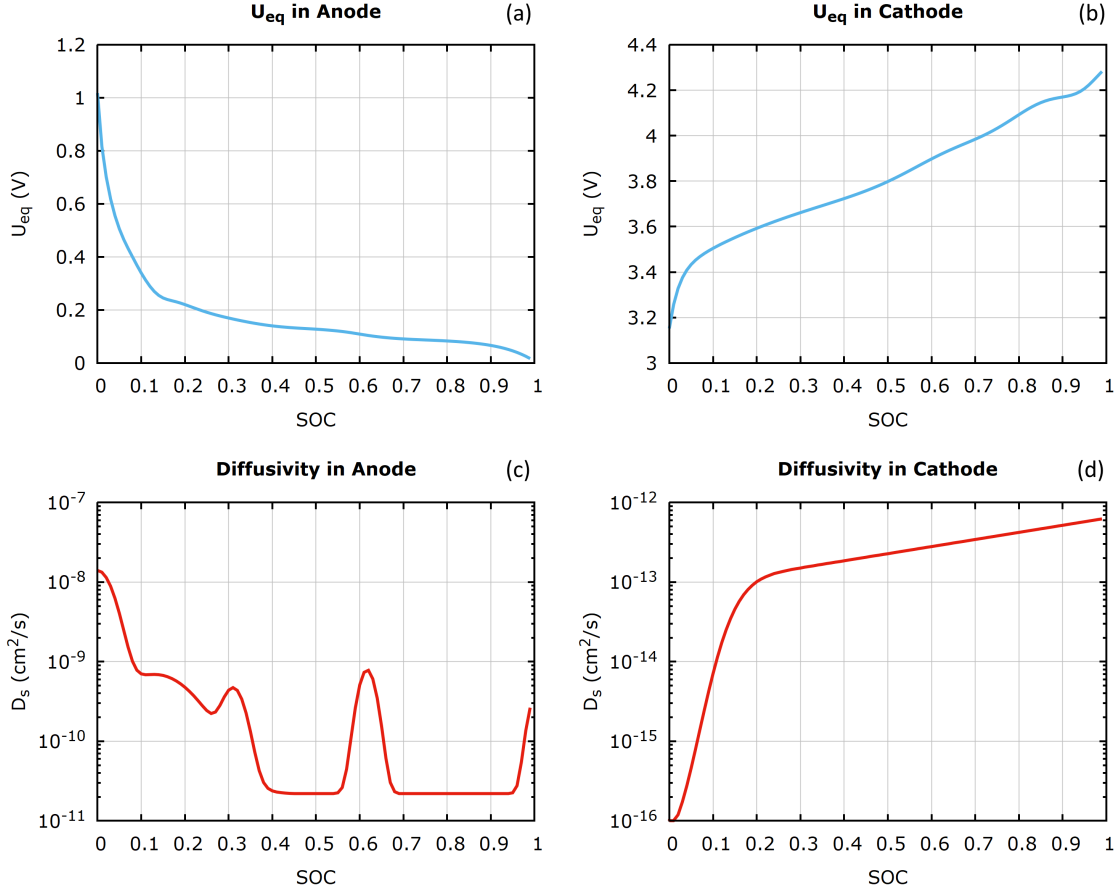
11

Figure 4: Equilibrium potentials of graphite anode (top left) and NCA cathode (top right), and diffusion coefficients in solid particles as a function of full cell SOC for anode (bottom left) and cathode (bottom right)

are obtained by averaging the pseudo-OCV curves for charge and discharge and are provided in Supplementary Material as well (Eqs. (SE1)-(SE2), Tables ST1 and ST2). We note that the hysteresis implied by the presence of different pseudo-OCVs for charge and discharge cannot be explained by the nonlinear diffusion model for lithium transport in the electrode particles but could be adequately modelled by a phase-field model as propounded in [29]. However this adds very significant extra computational complexity which is not justified by the relatively small degree of hysteresis.

Galvanostatic intermittent titration technique (GITT) was employed using 5 min titration pulses of 1.25 mA and 1.30 mA for the anode and cathode, respectively, with subsequent 45 min of relaxation. Diffusion coefficients were calculated based on Sand's equation as derived by Chang-Hui *et al.* [12]. All electrochemical tests including the validation experiments were performed using a Biologic BCS 815 system with the cells kept under air-cooling at 25°C (Spec PU2J) having their surface temperature monitored via K-type thermocouples in all experiments. The equilibrium potential is taken as the voltage obtained at C/25 (pseudo-OCV) and the full cell response is compared with the half cells for an evaluation of the individual electrode's utilisation in the full cell. In figure 4, the equilibrium potentials and diffusion coefficients for both electrodes are shown as a function of the SoC. By identifying the central graphite peak on the differential voltage analysis,[40] the anode-to-cathode ratio was estimated as 1.2. The initial and maximum concentrations of lithium on the particles were derived by fitting the full

cell voltage during low-current (C/25) discharge, and the reaction rate constants were obtained from fitting to the voltage profile obtained from the GITT experiment (see section 4 below). Additional constant parameters taken from the literature are the transference number and the conductivity of the solid, which are not expected to vary considerably in systems of similar chemical composition. The complete list of parameters used in our simulations can be found in Table 1.

4   Model fitting

For the purposes of the model, maximum and initial lithium concentration on the individual electrodes are independent inputs. Effectively, they represent an absolute quantity in moles of lithium per unit volume of active material and can be estimated theoretically if the true crystal density and stoichiometries are known. The maximum theoretical concentration of lithium in the cathode (c_c^{max}) can be calculated using the formula $c_c^{\mathrm{max}} = \rho z / \mu$, where z (the fraction of lithium per mole of cathode material) is 1 and the molar mass of the lithiated compound is found to be $\mu = 95.96$ g/mol. If we assume a crystal density of $\rho = 4.45$ g/cm^3 (NCA 80, CAS No. 193214-24-3), this yields a maximum lithium concentration of 46371 mol/m^3. For the anode material, we disregard the presence of SiOx and take the crystal density and molar mass of the lithiated graphite only, yielding a maximum lithium concentration in the anode of 25348 mol/m^3.

As disparities between the theoretical and practical values are to be expected, the identification of parameters is made unequivocally by fitting the DFN model to the pseudo-OCV experimental curves obtained at low current (C/25). This is accomplished by fitting initial and maximum concentrations so that the shape of the voltage versus the total capacity curve for the battery corresponds to the measured values as closely as possible. Using a good initial guess for the initial/maximum concentrations we performed a set of simulations with different $c_{a,0}$, $c_{c,0}$, c_a^{max} and c_c^{max} and by comparing the output voltage to the full cell measurement (with the aid of a root mean square deviation formula) adjusted the values of these parameters appropriately. The values obtained from such fitting (See Table 1) are remarkably similar and were used on our simulations. Initial concentration of Li in the particles are calculated in the same way - for simulating a discharge, initial Li concentration in the anode will be close to its maximum Li concentration, reflecting the almost fully lithiated state.

Likewise, initial guesses for the Butler-Volmer reaction rate constants for delithiation in the anode and lithiation in the cathode were taken from the COMSOL library of materials (Graphite MCBM: 2×10^{-11} and NCA-80: 5×10^{-10} m/s; COMSOL Multiphysics 5.4) and adjusted by fitting the DFN model output to the experimentally determined GITT curves. GITT consist in monitoring the voltage response upon a series of short current pulses followed by an extended relaxation phase, throughout the entire charge or discharge event. Using the appropriate values of current pulses and relaxation times, resistances and diffusion coefficients can be estimated as a function of a discrete number of SoCs [41, 42]. To reproduce a GITT experiment in DandeLiion [20], the user has to provide the desired profile of current versus time, following a square wave pattern of current either constant or zero. This is demonstrated in figure 6 where the input current is shown as a purple solid line, and the total voltage obtained numerically (red line) is compared with the experimental data (black line). Four zoomed-in fragments of the plot are given in figure 7. Our results clearly show excellent agreement, confirming that the model still captures the shape of the entire experimental total voltage profile as well as the shape of each voltage spike throughout the experiment from the beginning of discharge (figure 7, top left) till
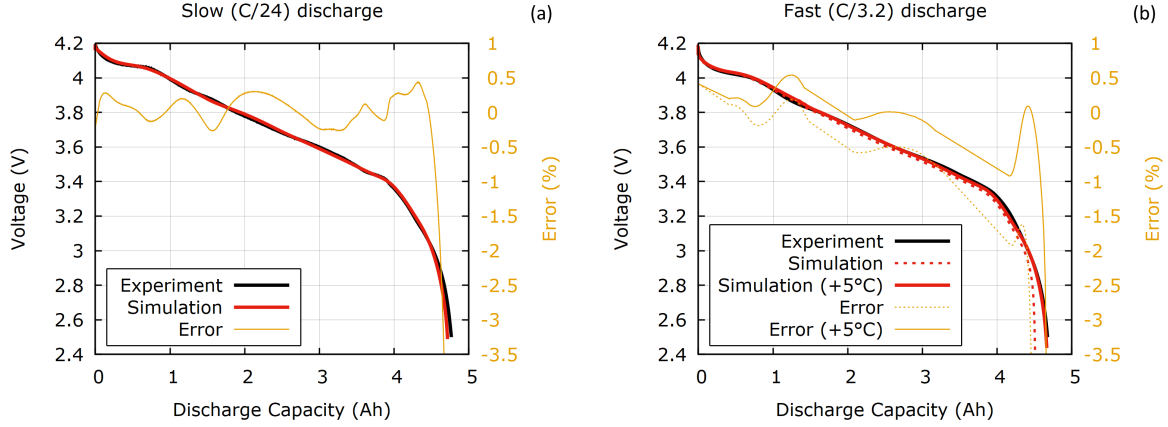
Figure 5: Constant current discharge curves for slow (C/24) discharge (a) and relatively fast (C/3.2) discharge (b). Simulation (red lines), experiment (black lines), and relative deviation of simulation results from the experiment (orange lines) are shown in time.

the end (figure 7, bottom right).

5 Results

After populating our parameters table, we solve the DFN model to predict the cell voltage from (i) a constant current discharge under different (slow and fast) discharge rates, and (ii) a drive cycle with a highly non-uniform current distribution. In all cases the initial conditions correspond to the fully pre-charged state (see initial concentrations of lithium in anode and cathode particle in table 1). The predictions were then compared to experimental results and used to estimate the absolute error between the cell voltage obtained from the fully parametrised model and that obtained from the equivalent experimental full-cell discharge.

5.1 Galvanostatic discharge

We investigated constant current discharges at a low rate, C/24 (200 mA), and at a higher rate, C/3.2 (1.5 A). The higher rate is the standard maximum discharge rate given in the battery specification, which if exceeded will likely result in a shortened battery lifetime of below 1,000 charge/discharge cycles. In both simulation and experiment the cell was discharged from full until the cell voltage dropped to the lower voltage limit, of 2.5 V, at which point it was considered fully discharged. While the C/24 discharge takes 24 hours, and is clearly slow, the C/3.2 discharge would still be considered relatively fast when compared to the standard discharge current rate, of C/5 (960 mA), that is found in the specification document (table 2).

Comparison of the simulation results against the experimental ones, for both constant current discharges, are made in figure 5. It can be seen that there is close agreement between the experimental and simulated total voltages curves, except for right at the end of the discharge this is less than 3%. The error is shown as the relative deviation on a voltage basis, calculated as $(V_{\text{Simulation}} - V_{\text{Experiment}})/V_{\text{Experiment}} \cdot 100\%$ at each point in time.

For both the slow and fast discharges we used an identical parameter set, which is given in table 1. For the slow discharge (figure 5, left plot), the relative error does not exceed 1%, except for the last few minutes of discharge when the battery is almost fully discharged. For the
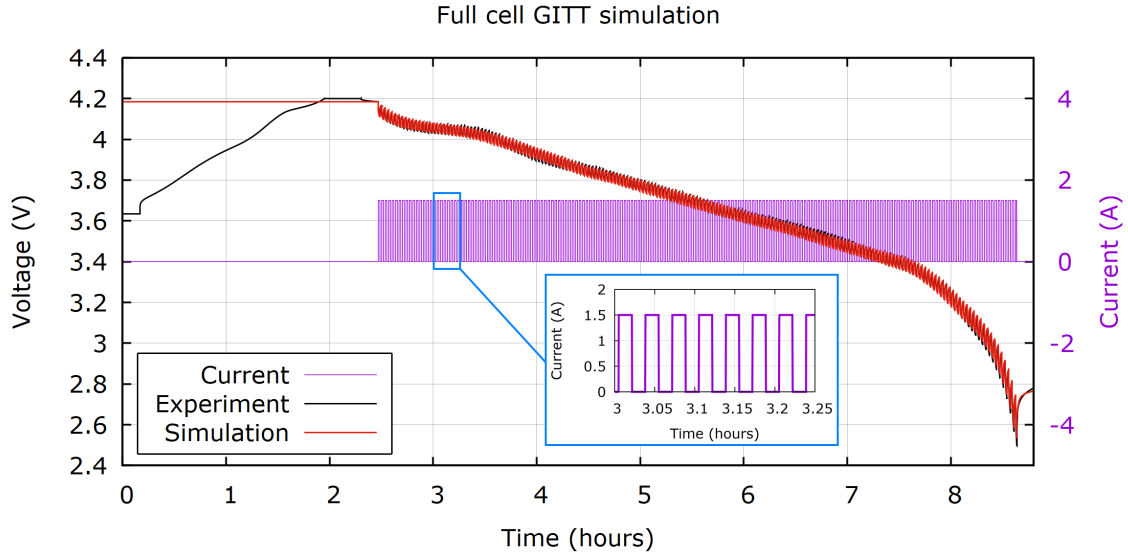
Figure 6: Full cell GITT simulation in comparison with the measurements. Full discharge profile and the current.

relatively fast discharge (figure 5, full agreement is seen in the initial first hour of test. However, with time, the model increasingly underestimates the voltage, although it is still within an acceptable error range. As the model considers isothermal conditions throughout the whole experiment (here at 25 °C), these deviations almost certainly result from the temperature increase seen in the middle-to-end of discharge; this is aggravated by increasing current. Self-heating of the batteries is negligible for low current discharges, *e.g.* C/24, but much more significant for higher rates, such as C/3.2. This is true even when the experiment is carried out in a thermal chamber [43], as shown in Figure S7. To account for the variations in temperature observed experimentally, we display the simulated discharge profile for C/3.2 and at 30°C, and significantly improved agreement between prediction and experiment (see figure 5 b, solid lines).

5.2   Drive cycles

In contrast to laboratory measurements where a constant current, or series of constant current pulses, is typically applied to a cell in order to characterise its performance, the operation of batteries in real world applications gives rise to highly non-uniform loads. From an application point of view, it is imperative that physics-based models can reproduce battery behaviour during practical operation say, for example, in electric vehicles. In order to illustrate the use of our parametrised model under conditions akin to that in the operation of an electric vehicle we simulate battery performance when subject to a drive cycle load based on a standardized test protocol. Figure 8 shows the current patterns for a single-commute time based on a world harmonized light-duty vehicles test procedure (WLTP, class 3, version acceleration [44]), which we used to validate our model. Again, the same set of parameters used in the previous simulations (table 1) are used to simulate a drive-cycle pattern based on the periodic repetition of the current pattern shown in figure 8. Simulation results for the cell voltage (red) are compared to experimental ones (black) in figure 9. The relative error is shown in yellow. The top plot shows the entire discharge cycle, comprised of the periodically repeated current pattern plotted in Fig. 8), from the fully pre-charged state until the cell is fully discharged (*i.e.* when the cell voltage drops to 2.5 V). Figure 9(b) and (c) are two 1/2 hour fragments of the top plot, which
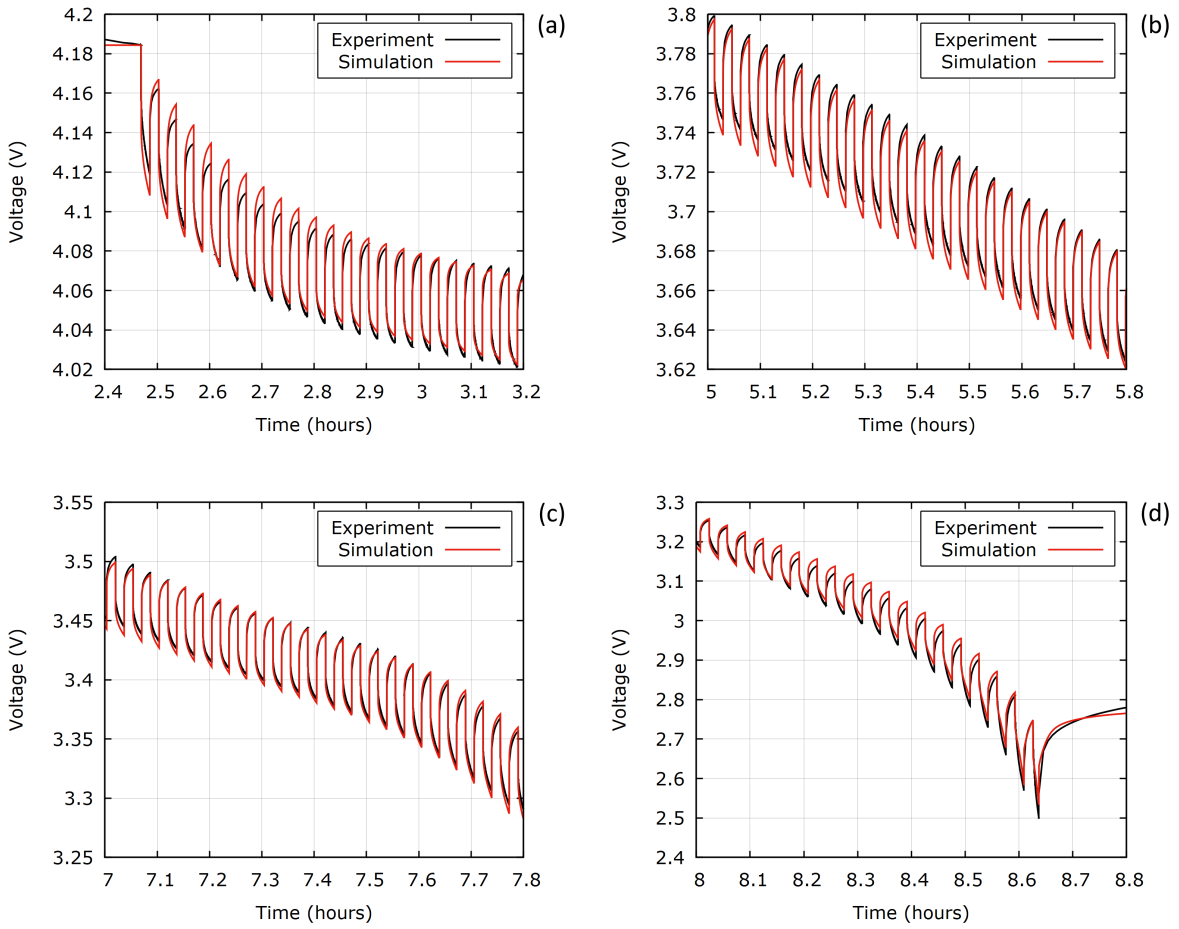
Figure 7: Four fragments of the full discharge curve shown in Figure 6. Beginning of discharge (a), middle of discharge (b), near the end of discharge (c), and at the end of the experiment (d).
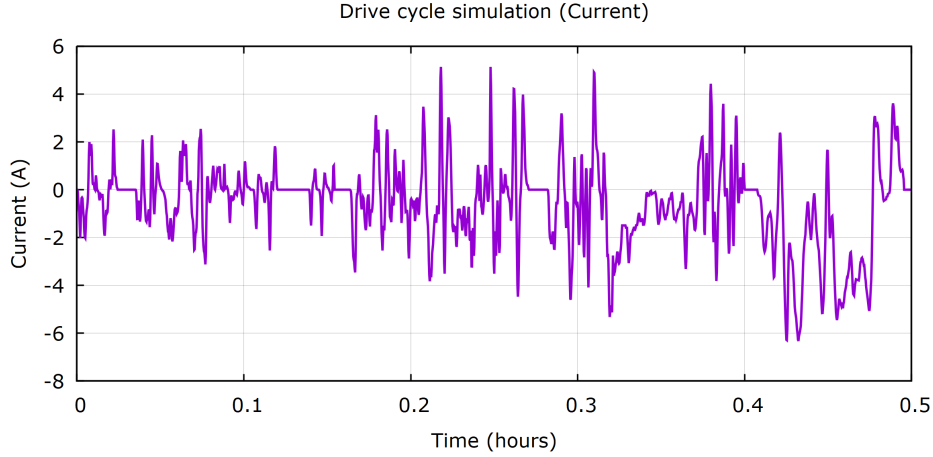
Figure 8: A single pattern of the total current that mimics a drive cycle of an electric vehicle.

correspond to approximately the middle and the end of discharge. According to the plots, the model reproduces experimental data with a very high accuracy over the whole discharge interval. The relative error does not exceed 2% except in the last few minutes of discharge (out of 7.5 hours) when the battery is almost fully discharged and the total voltage fluctuations increase. Again, the deviation at the end of discharge can be attributed to a non-negligible increase in battery temperature due to self-heating.

5.3 Energy dissipation

The results in the §5.1 and §5.2 demonstrate that remarkably good agreement can be obtained between a properly calibrated DFN model and experiment. This should give the user confidence that the DFN model provides a very good approximation of the physical and electrochemical processes occurring within the battery. A natural question to ask is how the information gained by performing a careful, but relatively costly and time consuming, parametrisation can be leveraged to improve its design and usage. Since lithium-ion batteries are energy storage devices a key indicator of their efficiency, for a particular task, is the size and location of the energy dissipation occurring within the device. Indeed this is a good way of assessing the fitness of the cell for a particular purpose and of improving its design. A recent rigorous mathematical analysis of the DFN model [28] has been used to develop and exact energy conservation law for a device described by the DFN model, which shows that GA, the Gibbs free energy of a cell of area A, evolves according to an energy conservation law of the form

$$-A\frac{dG}{dt} = IV + A\left(\dot{\mathcal{Q}}^{\text{(elyte)}} + \dot{\mathcal{Q}}^{\text{(a)}}_{\text{part.}} + \dot{\mathcal{Q}}^{\text{(a)}}_{\text{ohm}} + \dot{\mathcal{Q}}^{\text{(a)}}_{\text{pol.}} + \dot{\mathcal{Q}}^{\text{(c)}}_{\text{part.}} + \dot{\mathcal{Q}}^{\text{(c)}}_{\text{ohm}} + \dot{\mathcal{Q}}^{\text{(c)}}_{\text{pol.}}\right). \qquad (16)$$

Here IV (current times voltage) is the useful power extracted from the cell while the terms bracketed on the right-hand side of this equation are the irreversible energy losses (per unit area of cell and per unit time). These terms have been divided up into seven location within the cell, where losses can occur, see Table 3; thus $\dot{\mathcal{Q}}^{\text{(elyte)}}$ is the loss in the electrolyte, $\dot{\mathcal{Q}}^{\text{(a)}}_{\text{part.}}$ is that due to the heat of mixing in the anode particles, $\dot{\mathcal{Q}}^{\text{(a)}}_{\text{ohm}}$ is that due to Ohmic losses in the carbon binder domain in the anode, $\dot{\mathcal{Q}}^{\text{(a)}}_{\text{pol.}}$ are the polarisation losses resulting from the overpotential between the anode particles and the surrounding electrolyte, $\dot{\mathcal{Q}}^{\text{(c)}}_{\text{part.}}$ is that due to the heat of mixing in the cathode particles, $\dot{\mathcal{Q}}^{\text{(c)}}_{\text{ohm}}$ is that due to Ohmic losses in the carbon binder domain
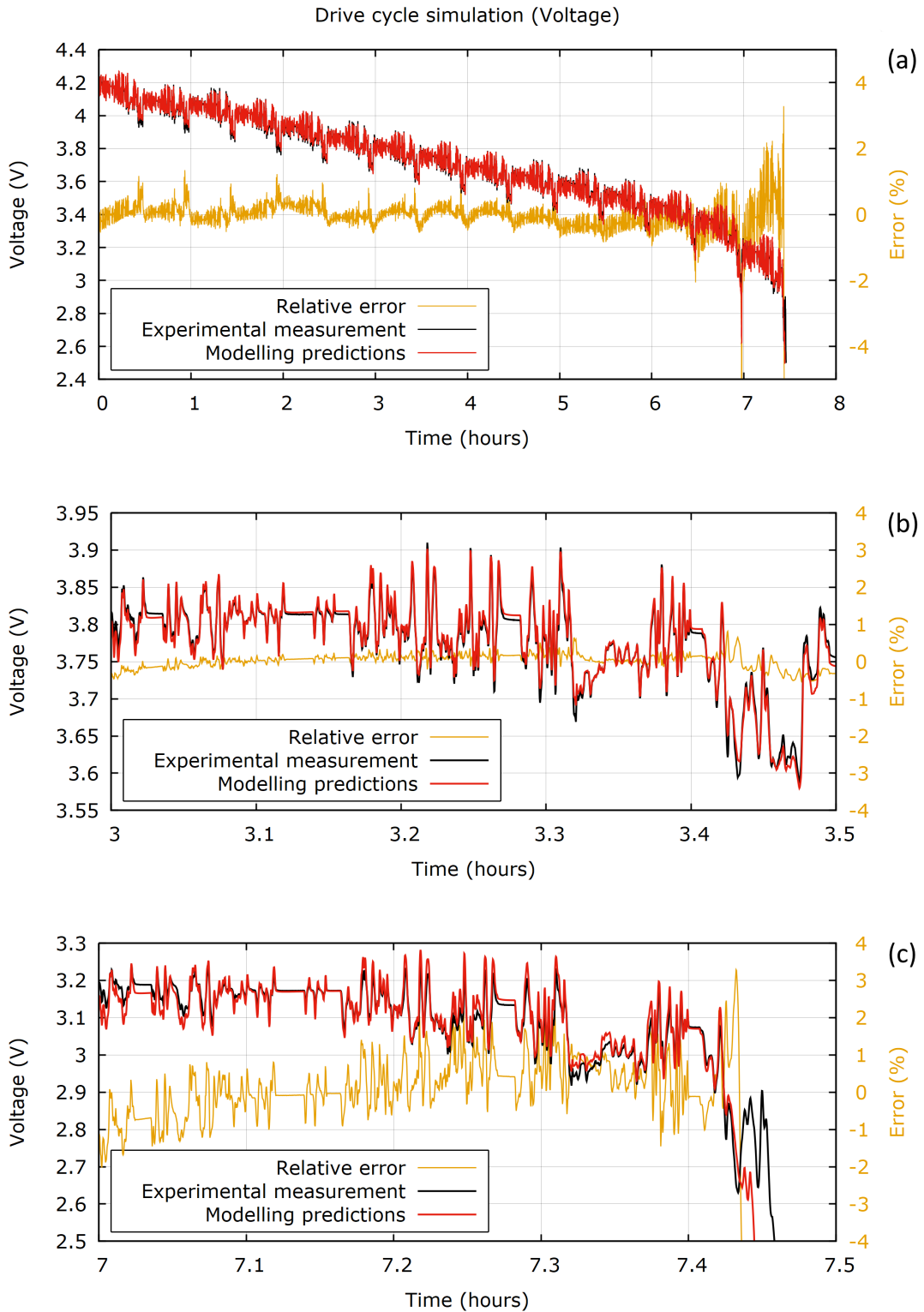
17

Figure 9: Drive cycle simulation full discharge curve in comparison with the experiment (a), and two zoomed-in fragments in the middle of discharge (b) and at the very end of discharge (c). Orange line is the relative deviation of simulation results from the experiment.

18

in the cathode, $\dot{\mathcal{Q}}_{\text{pol.}}^{(c)}$ are the polarisation losses resulting from the overpotential between the cathode particles and the surrounding electrolyte. In [28] it is shown how these loss terms should be computed from integrals of the solution to the DFN model so that equation (16) is satisfied exactly. Notably, the result obtained in [28] differs significantly from the standard (and incorrect) methods that have been used to compute the irreversible energy losses from solutions to the DFN model.

All the heating terms in equation (16) are summarised in Table 3, where the dissipative effects in the electrolyte $\dot{\mathcal{Q}}^{(\text{elyte})}$ and the heat of mixing in particles ($\dot{\mathcal{Q}}_{\text{part.}}^{(a)}$ and $\dot{\mathcal{Q}}_{\text{part.}}^{(c)}$) can be expressed via the following integrals:

$$\dot{\mathcal{Q}}^{(\text{elyte})} = \int_{L_1}^{L_4} \left(2\mathcal{B}(x) D_e(c) \frac{d\mu_e}{dc} \left(\frac{\partial c}{\partial x} \right)^2 + \frac{1}{\kappa(c)\mathcal{B}(x)} \langle j \rangle^2 \right) dx, \qquad (17)$$

$$\dot{\mathcal{Q}}_{\text{part.}}^{(a)} = -4\pi F \int_{L_1}^{L_2} \frac{b(x)}{4\pi R_a^2(x)} \left(\int_0^{R_a(x)} D_a(c_a) \left(\frac{\partial c_a}{\partial r} \right)^2 \frac{dU_{eq,a}}{dc_a} r^2 dr \right) dx, \qquad (18)$$

$$\dot{\mathcal{Q}}_{\text{part.}}^{(c)} = -4\pi F \int_{L_3}^{L_4} \frac{b(x)}{4\pi R_c^2(x)} \left(\int_0^{R_c(x)} D_c(c_c) \left(\frac{\partial c_c}{\partial r} \right)^2 \frac{dU_{eq,c}}{dc_c} r^2 dr \right) dx, \qquad (19)$$

where $\mu_e(c)$ is the chemical potential of the electrolyte and $\langle j \rangle$ is the averaged electrolyte current density. The current $\bar{j}_n$ in Table 3 is the component of current density on electrode particle surface in direction of outward normal to particle. The rest of the parameters were introduced in section 2 above.

Table 3: A summary of all heat dissipation terms used in the energy conservation law (16)

| No.	Term	Description	Formula
1	$\dot{\mathcal{Q}}^{(\text{elyte})}$	Dissipative effects in the electrolyte	(17)
2	$\dot{\mathcal{Q}}_{\text{part.}}^{(a)}$	The heat of mixing in the anode particles	(18)
3	$\dot{\mathcal{Q}}_{\text{part.}}^{(c)}$	The heat of mixing in the cathode particles	(19)
4	$\dot{\mathcal{Q}}_{\text{ohm}}^{(a)}$	Ohmic dissipation in the solid parts of the anode	$\dot{\mathcal{Q}}_{\text{ohm}}^{(a)} = \int_{L_1}^{L_2} \sigma_a \left(\frac{\partial \Phi_a}{\partial x} \right)^2 dx$
5	$\dot{\mathcal{Q}}_{\text{ohm}}^{(c)}$	Ohmic dissipation in the solid parts of the cathode	$\dot{\mathcal{Q}}_{\text{ohm}}^{(c)} = \int_{L_3}^{L_4} \sigma_c \left(\frac{\partial \Phi_c}{\partial x} \right)^2 dx$
6	$\dot{\mathcal{Q}}_{\text{pol.}}^{(a)}$	The polarisation losses at the surfaces of the anode particles	$\dot{\mathcal{Q}}_{\text{pol.}}^{(a)} = \int_{L_1}^{L_2} b(x)\eta_a \bar{j}_n dx$
7	$\dot{\mathcal{Q}}_{\text{pol.}}^{(c)}$	The polarisation losses at the surfaces of the cathode particles	$\dot{\mathcal{Q}}_{\text{pol.}}^{(c)} = \int_{L_3}^{L_4} b(x)\eta_c \bar{j}_n dx$
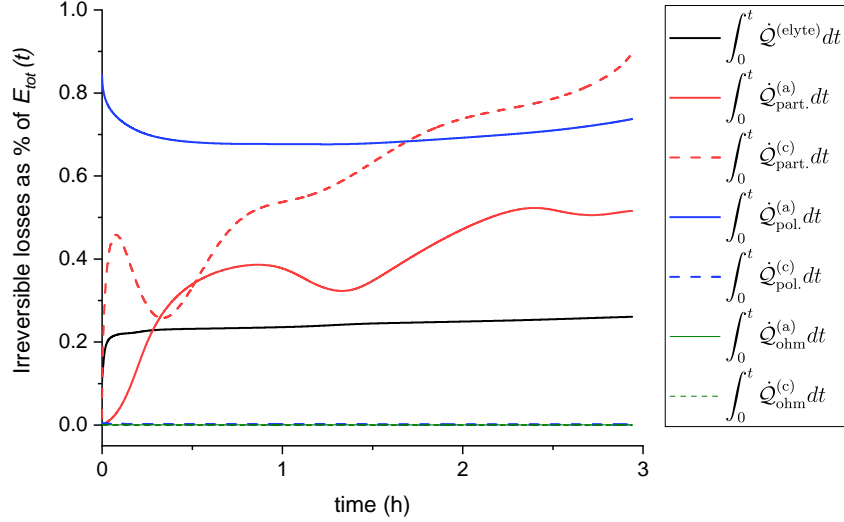
Figure 10: Cumulative irreversible energy losses (per unit area of cell) as a percentage of $E_{tot}(t)$ the cumulative energy use (per unit area of cell) for constant current (C/3.2) discharge.

In figures 10 and 11 we show the cumulative energy losses (per unit area), for both C/3.2 constant current discharge and drive cycle, as a percentage of $E_{tot}(t)$ the total chemical energy consumed by the cell (per unit area) throughout the discharge, until time t, as defined by the relation

$$E_{tot}(t) = \int_0^t \left\{ \frac{IV}{A} + \left(\dot{Q}^{(\text{elyte})} + \dot{Q}_{\text{part.}}^{(a)} + \dot{Q}_{\text{ohm}}^{(a)} + \dot{Q}_{\text{pol.}}^{(a)} + \dot{Q}_{\text{part.}}^{(c)} + \dot{Q}_{\text{ohm}}^{(c)} + \dot{Q}_{\text{pol.}}^{(c)} \right) \right\} dt, \quad (20)$$

or equivalently (on using the identity (16)) $E_{tot}(t) = G(0) - G(t)$. In figure 12b we show the the cumulative electrical work (per unit area) done by the cell as a percentage of $E_{tot}(t)$ the total chemical energy consumed by the cell (per unit area).

Notably in both cases, constant current discharge and drive cycle, this is a fairly efficient cell which which only loses roughly 2.5% and 4% of its chemical energy irreversibly. However, it is still interesting to compare where these losses predominantly occur within the cell. For the constant current discharge, the dominant losses are heat of mixing in the cathode particles (a term usually neglected in standard treatments of heating in Li-ion batteries) and polarisation losses in the anode. In contrast, for the drive cycle polarisation losses in the anode, are by some distance, the most pronounced source of unwanted energy dissipation.

6   Conclusion

In this work we have shown that a carefully parametrised DFN model is capable of accurately predicting the behaviour of a cell for a wide variety of cell discharges and, in particular, could accurately predict cell voltage profiles during both galvanostatic and drive-cycles discharges. We were also able to use the solutions to the DFN model to accurately compute the irreversible energy losses occurring within the cell, for different discharge patterns, and infer their location. In performing these tasks, we have shown that such well-parametrised DFN models are an extremely useful engineering tool to support control systems or to inform new cell designs. In particular knowledge of the location of the major energy losses can be used to point to components of the cell that should be redesigned. We illustrated a simplified experimental workflow to effectively extract the model key parameters from a physical cell. This was based upon a careful
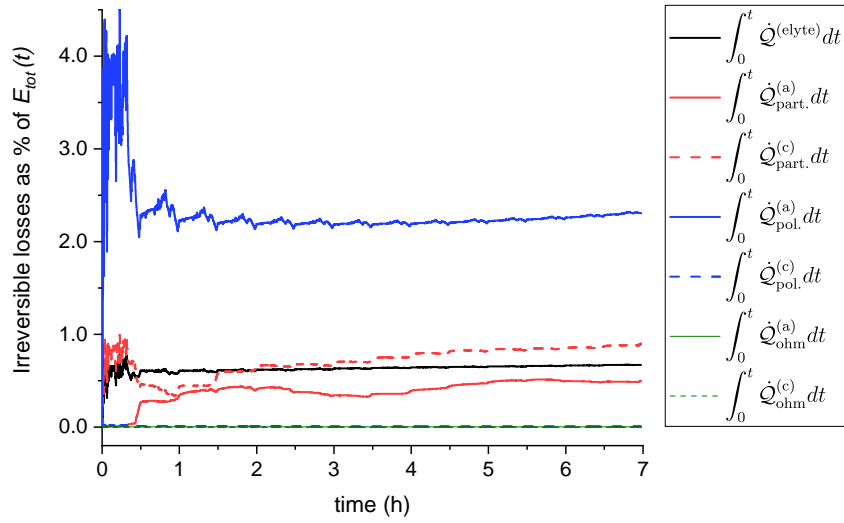
Figure 11: Cumulative irreversible energy losses (per unit area of cell) as a percentage of $E_{tot}(t)$ the cumulative energy use (per unit area of cell) for drive cycle simulation.
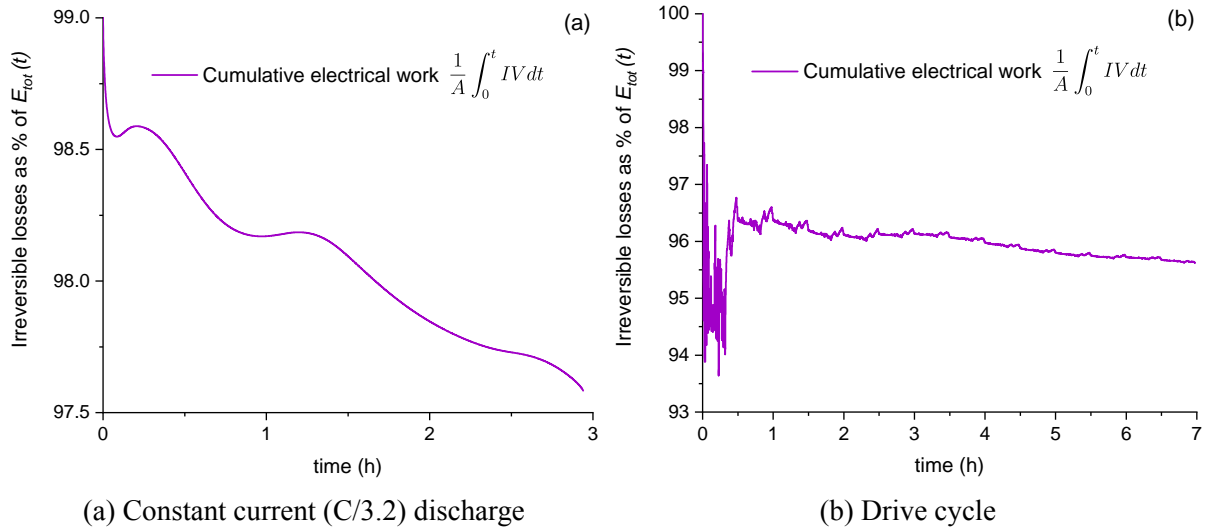

(a) Constant current (C/3.2) discharge

(b) Drive cycle

Figure 12: Cumulative electrical work (per unit area of cell) $\int_0^t IV/A\,dt$ as a percentage of $E_{tot}(t)$, the cumulative energy use (per unit area of cell), for (a) constant current (C/3.2) discharge and (b) drive cycle simulation.

assessment of the critical parameters that most influence the cell's behaviour; these turn out to be those that are related to its total capacity and its transport properties (*e.g.* particle radius, electrode thicknesses, active material content and diffusion coefficients). Finally, we remark that DandeLiion solver has the potential to be leveraged for on-board battery management systems in electric vehicles and used to perform real time computations, given its sub-second timescale resolution.

References

[1] M. Doyle, T. F. Fuller, & J. Newman, *Modeling of galvanostatic charge and discharge of the lithium polymer insertion cell*, J. Electrochem. Soc., 140 (1993), pp. 1526–1533.

[2] M. Doyle, J. Newman, A. S. Gozdz, C. N. Schmutz, & J.-M. Tarascon, *Comparison of modeling predictions with experimental data from plastic lithium ion cells*, J. Electrochem. Soc., 143 (1996), pp. 1890–1903.

[3] T. F. Fuller, M. Doyle, & J. Newman, *Simulation and optimization of the dual lithium ion insertion cell*, J. Electrochem. Soc., 141 (1994), pp. 1–10.

[4] G.L. Plett, *Battery Management Systems, Volume II: Equivalent-Circuit Methods*, Artech House, 2015.

[5] A.X. Hu, S. Li, & H. Peng , *A comparative study of equivalent circuit models for Li-ion batteries*, J. Power Sources. 198 (2012) 359–367.

[6] J. Newman, & K. E. Thomas-Alyea , *Electrochemical Systems 3rd Edition*, Wiley 2014.

[7] J. Newman, K.E. Thomas, H. Hafezi, & D.R. Wheeler, *Modeling of lithium-ion batteries*, J. Power Sources. 119–121 (2003) 838–843.

[8] A. Latz & J. Zausch. *Multiscale modeling of lithium ion batteries: thermal aspects.* Beilstein Journal of Nanotechnology, 6, 987–1007, 2015.

[9] Y. Li, K. Liu, A.M. Foley, A. Zülke, M. Berecibar, E. Nanini-Maury, J. Van Mierlo, & H.E. Hoster, *Data-driven health estimation and lifetime prediction of lithium-ion batteries: A review*, Renew. Sustain. Energy Rev. 113 (2019) 109254.

[10] J.C. Forman, S.J. Moura, J.L. Stein, & H.K. Fathy, *Genetic identification and fisher identifiability analysis of the Doyle–Fuller–Newman model from experimental cycling of a $LiFePO_4$ cell*, J. Power Sources, 210 (2012) pp. 263–275.

[11] A. Maheshwari, M.A. Dumitrescu, M. Destro, & M. Santarelli, *Inverse parameter determination in the development of an optimized lithium iron phosphate - Graphite battery discharge model*, J. Power Sources, 307 (2016), pp. 160–172.

[12] C.-H. Chen, F. Brosa Planella, K. O'Regan, D. Gastol, W.D. Widanage & E. Kendrick, *Development of Experimental Techniques for Parameterization of Multi-scale Lithium-ion Battery Models*, J. Electrochem. Soc. 167 (2020) 080534.

[13] M. Kim, H. Chun, J. Kim, K. Kim, J. Yu, T. Kim, & S. Han, *Data-efficient parameter identification of electrochemical lithium-ion battery model using deep Bayesian harmony search*, Appl. Energy., **254**, (2019).

[14] S. Park, D. Kato, Z. Gima, R. Klein, & S. Moura, *Optimal Experimental Design for Parameterization of an Electrochemical Lithium-Ion Battery Model*, J. Electrochem. Soc., **165**, (2018) A1309–A1323.

[15] J. Sturm, A. Rheinfeld, I. Zilberman, F.B. Spingler, S. Kosch, F. Frie, & A. Jossen, *Modeling and simulation of inhomogeneities in a 18650 nickel-rich, silicon-graphite lithium-ion cell during fast charging*, J. Power Sources, **412**, (2019) 204–223.

[16] K. Uddin, S. Perera, W.D. Widanage, L. Somerville, & J. Marco, *Characterising lithium-ion battery degradation through the identification and tracking of electrochemical battery model parameters*, Batteries, **2**, (2016).

[17] S. Santhanagopalan, Q. Guo, & R.E. White,, *Parameter estimation and model discrimination for a lithium-ion cell.*, J. Electrochem. Soc., **154**, (2007) A198–A20.

[18] L. Oca, E. Miguela, E. Agirrezabala, A. Herran, E. Gucciardi, L. Otaegui, E. Bekaert, A. Villaverde, & U. Iraola, *Physico-chemical parameter measurement and model response evaluation for a pseudo-two-dimensional model of a commercial lithium-ion battery*, Electrochimica Acta, 382 (2021), 138287.

[19] M. Ecker, T. K. D. Tran, P. Dechent, S. Käbitz, A. Warnecke, & D. U. Sauer, *Parameterization of a physico-chemical model of a lithium-ion battery. I. Determination of parameters*, J. Electrochem. Soc., **162**, (2015), pp. A1836–A1848.

[20] DandeLiion online simulation engine, `https://www.dandeliion.com/`

[21] I. Korotkin, S. Sahu, S. E. J. O'Kane, G. Richardson, & J. M. Foster, *DandeLiion v1: An extremely fast solver for the Newman model of lithium-ion battery (dis)charge*, J. Electrochem. Soc., 168 (2021), 060544.

[22] J.M. Reniers, G. Mulder, & D.A. Howey,, *Unlocking extra value from grid batteries using advanced models*, J. Power Sources 487 (2021) 229355.

[23] A. Allam, E. Catenaro, & S. Onori,, *Pushing the Envelope in Battery Estimation Algorithms*, iScience 23, (2020).

[24] M. Ecker, S. Käbitz, I. Laresgoiti, & D. U. Sauer, *Parameterization of a physico-chemical model of a lithium-ion battery. II. Model validation*, J. Electrochem. Soc., **162**, (2015), pp. A1849–A1857.

[25] Kang-Joon ParkKang-Joon Park, Jang-Yeon Hwang, Hoon-Hee Ryu, Filippo Maglia, Sung-Jin Kim, Peter Lamp, Chong S. Yoon, & Yang-Kook Sun, *Degradation Mechanism of Ni-Enriched NCA Cathode for Lithium Batteries: Are Microcracks Really Critical?*, ACS Energy Lett. 4, 1394–1400 (2019).

[26] F. Ciucci & W. Lai, *Derivation of micro/macro lithium battery models from homogenization*, Transport in Porous Media, 88 (2011),pp. 249–270.

[27] G. Richardson, G. Denuault, & C. Please, *Multiscale modelling and analysis of lithium-ion battery charge and discharge*, J. Eng. Maths., 72 (2012), pp. 41–72.

[28] G. Richardson, & I. Korotkin. *Heat Generation and a Conservation Law for Chemical Energy in Li-ion batteries.* Electrochimica Acta, **392**, (2021) 138909.

[29] Y. Zeng & M.Z. Bazant, *Phase separation dynamics in isotropic ion-intercalation particles*, SIAM J. Appl. Math., 74(4), pp. 980–1004, 2014.

[30] J.W. Cahn & J.E. Hilliard, *Free energy of a nonuniform system. I. Interfacial freeenergy*, J. Chem. Phys., 28(2), pp. 258–267, 1958.

[31] J.W. Cahn, *Free energy of a nonuniform system. II. Thermodynamic basis*, J. Chem. Phys., 30(5), pp. 1121–1124, 1959.

[32] J.W. Cahn, & J.E. Hilliard, *Free energy of a nonuniform system. III. Nucleation in a two-component incompressible fluid*, J. Chem. Phys., 31(3), pp. 688–699, 1959.

[33] M.W. Verbrugge & B.J. Koch, *Modeling lithium intercalation of single fiber carbon microelectrodes.* J. Electrochem. Soc. 143, (1996) 600-608.

[34] S. A. Krachkovskiy, J. M. Foster, J. D. Bazak, B. J. Balcom, & G. R. Goward, *Operando mapping of Li concentration profiles and phase transformations in graphite electrodes by magnetic resonance imaging and nuclear magnetic resonance spectroscopy*, J. Phys. Chem. C, 122, no. 38 (2018): 21784-21791.

[35] W. Li, D. Cao, D. Jöst, F. Ringbeck, M. Kuipers, F. Friea, & D. Uwe Sauer, *Parameter sensitivity analysis of electrochemical model-based battery management systems for lithium-ion batteries*, Appl. Energy. 269 (2020) 115104.

[36] R.M. Burrell, A.A. Zulke, P. Keil, & H. Hoster, *Communication—Identifying and Managing Reversible Capacity Losses that Falsify Cycle Ageing Tests of Lithium-Ion Cells*, J. Electrochem. Soc. 167 (2020) 130544.

[37] B. D. Bruggeman, *Calculation of different physical constants of heterogeneous substances. i. dielectric constants and conductivities of mixed bodies of isotropic substances*, Annalen der Physik, **416**, (1935), pp. 636–664.

[38] J. Landesfeind, J. Hattendorff, A. Ehrl, W.A. Wall & H.A. Gasteiger, *Tortuosity Determination of Battery Electrodes and Separators by Impedance Spectroscopy.* J. Electrochem. Soc. 167, A1373-A1387 (2016).

[39] A. Latz & J. Zausch. *Thermodynamic consistent transport theory of Li-ion batteries.* Journal of Power Sources, 196, 3296–3302, (2011).

[40] M.P. Mercer, M. Otero, M. Ferrer-Huerta, A. Sigal, D.E. Barraco, H.E. Hoster, E.P.M. Leiva, *Transitions of lithium occupation in graphite: A physically informed model in the dilute lithium occupation limit supported by electrochemical and thermodynamic measurements.*, Electrochim. Acta. 324 (2019) 134774.

[41] Y. Zhu & C. Wang, *Galvanostatic intermittent titration technique for phase-transformation electrodes*, J. Phys. Chem. C. 114 (2010) 2830–2841.

[42] A. Nickol, T. Schied, C. Heubner, M. Schneider, A. Michaelis, M. Bobeth, & G. Cunibertid, *GITT Analysis of Lithium Insertion Cathodes for Determining the Lithium Diffusion Coefficient at Low Temperature: Challenges and Pitfalls*, J. Electrochem. Soc. 167 (2020) 090546.

[43] A. Zülke, Y. Li, P. Keil, & H. Hoster, *Communication—Why High-Precision Coulometry and Lithium Plating Studies on Commercial Lithium-Ion Cells Require Thermal Baths*, J. Electrochem. Soc. 166 (2019) A2921–A2923.

[44] UNECE Global technical regulation No 15 (GTR 15), *WP.29, Proposal for a new global technical regulation on the Worldwide harmonized Light vehicles Test Procedure (WLTP)*, World Forum Harmon. Veh. Regul. 2016 (2014) 237.